Adaptive Simulations of Two-Phase Flow by Discontinuous Galerkin Methods

W. Klieber and B. Rivière *,1

Department of Mathematics, University of Pittsburgh, 301 Thackeray, Pittsburgh, PA 15260, U.S.A.

Abstract

In this paper we present a non-symmetric interior penalty Galerkin formulation of the two-phase flow equations. The wetting phase pressure and saturation equations are decoupled and solved sequentially. Proposed adaptivity in space and time techniques yield accurate and efficient solutions. Slope limiters valid on nonconforming meshes are also presented. Numerical examples of homogeneous and heterogeneous media are considered.

Key words: error indicators, discontinuous Galerkin, adaptive time stepping, slope limiters, five-spot, high order,

1 Introduction

Accurate simulations of multiphase processes are essential in problems related to the environment and the energy. There is a need for discretization methods that perform well on very general unstructured grids. Standard methods such as the finite difference methods, finite volumes and expanded mixed finite element fail to capture the flow phenomena in the case of highly heterogeneous media with full permeability tensors. Recently, discontinuous Galerkin (DG) methods have been applied to a variety of flow and transport problem [13,14,1,15] and due to their flexibility, they have been shown to be competitive to standard methods. Furthermore, DG methods allow for unstructured

* Corresponding author: Tel: 412-6248315, Fax: 412-6248397
Email address: riviere@math.pitt.edu (W. Klieber and B. Rivière).

[1] The first author was partially supported by a CRDF grant from the University of Pittsburgh and by a Brackenridge fellowship. The second author was supported by a National Science Foundation grant DMS-0506039.

meshes and full tensor coefficients. Even though the discontinuous finite element methods are more expensive than the finite difference methods, oil engineers are willing to pay the price for accuracy and thus avoid costly mistakes [12].

In this work, the pressure-saturation formulation (also known as the IMPES formulation) of the two-phase flow problem is discretized using the non-symmetric interior penalty Galerkin method (NIPG). The unknowns are the wetting phase pressure and saturation and the equations are solved sequentially. One immediate advantage of the IMPES formulation is the fact that the difficulty arising from the nonlinearity is removed by time-lagging the coefficients.

The objective of this work is to investigate adaptive simulations in time and space. We formulate error indicators for the spatial refinement and derefinement techniques. We also present an algorithm that allows the time step to vary during the simulation. One of the main difficulties is the development of slope limiters that would handle meshes with hanging nodes. We propose a limiting technique based on the one introduced by Durlofsky et al [6] for conforming meshes. To our knowledge, there is little work in the literature on applications of DG methods to two-phase flow. In [3], simulations were performed on uniformly refined meshes and with a constant time step. In [2], DG is applied to a total pressure-saturation formulation. In [11], DG and mixed finite elements are coupled. In [7], fully coupled DG formulations are considered and in this case slope limiters are not needed even for high order of approximation. However, the solution of the fully coupled DG formulations require the construction of a Jacobian matrix at each time step for the Newton-Raphson method.

The plan of the paper is as follows. In the next section, we present the equations describing the two-phase flow problem. Section 3 contains the discrete scheme and notation. The adaptive strategy in space and time, as well as the slope limiting technique, are described in Section 4. Numerical examples are given in Section 5. Some conclusions follow.

2 Model Problem

The mathematical formulation of two-phase flow in a porous medium Ω in $\mathbb{R}^2$ consists of a coupled system of non-linear partial differential equations. The phases considered here are a wetting phase (such as water) and a non-wetting phase (such as oil). For each phase, the conservation of mass and a generalized Darcy's law are obtained. Under the assumption of incompressibility, a pressure-saturation formulation is derived, for which the primary variables are

the pressure and the saturation of the wetting phase denoted by p_w and s_w:

$$-\nabla \cdot (\lambda_t \boldsymbol{K} \nabla p_w) = \nabla \cdot (\lambda_o \boldsymbol{K} \nabla p_c), \tag{1}$$

$$\frac{\partial(\phi s_w)}{\partial t} + \nabla \cdot \left(\frac{\lambda_o \lambda_w}{\lambda_t} \boldsymbol{K} \nabla p_c \right) = -\nabla \cdot \left(\frac{\lambda_w}{\lambda_t} \boldsymbol{u}_t \right). \tag{2}$$

The coefficients in Equations (1) and (2) are defined below:

- $\boldsymbol{K}$ is the permeability tensor and is spatially dependent; for heterogeneous media, $\boldsymbol{K}$ is discontinuous.
- The coefficient ϕ denotes the porosity of the medium.
- $\lambda_t = \lambda_o + \lambda_w$ is the total mobility, that is, the sum of the mobility of the non-wetting phase and the mobility of the wetting phase. Mobilities are functions that depend on the fluid viscosities μ_w and μ_o and on the effective wetting phase saturation s_e. The effective saturation depends on the the residual wetting phase and non-wetting phase saturations s_{rw} and s_{ro} as follows:
$$s_e = \frac{s_w - s_{rw}}{1.0 - s_{rw} - s_{rn}}.$$
The mobilities are then given by the Brooks-Corey model [4]:
$$\lambda_w(s_w) = \frac{1}{\mu_w} s_e^4, \quad \lambda_o(s_w) = \frac{1}{\mu_o}(1 - s_e)^2(1 - s_e^2).$$
- The difference of the pressures of the two phases $p_c = p_n - p_w$ is the capillary pressure. From the Brooks-Corey model, it depends on the effective saturation and a constant entry pressure p_d:
$$p_c(s_w) = \frac{p_d}{\sqrt{s_e}}.$$
From this equation, we see that $p_c'(s_w) < 0$ and we will write: $\nabla p_c = -|p_c'| \nabla s_w$.
- $\boldsymbol{u}_t = \boldsymbol{u}_o + \boldsymbol{u}_w$ is the total velocity, that is the sum of the two phases velocities. Each phase velocity is given as:
$$\boldsymbol{u}_\delta = -\boldsymbol{K} \lambda_\delta \nabla p_\delta, \quad \delta = o, w.$$

Let $\boldsymbol{n}$ denote the outward normal to $\partial\Omega$. We associate to Equations (1) and (2) several boundary conditions, by first decomposing the boundary of the porous medium $\partial\Omega$ into disjoint parts:

$$\partial\Omega = \Gamma_{p1} \cup \Gamma_{p2} = \Gamma_{s1} \cup \Gamma_{s2}, \quad \Gamma_{p1} \cap \Gamma_{p2} = \Gamma_{s1} \cap \Gamma_{s2} = \emptyset.$$

The boundary conditions for (1) are of Dirichlet and Neumann type:

$$p_w = p_{\text{dir}}, \quad \text{on} \quad \Gamma_{p1}, \tag{3}$$

$$\boldsymbol{K} \lambda_t \nabla p_w \cdot \boldsymbol{n} = 0, \quad \text{on} \quad \Gamma_{p2}. \tag{4}$$

The boundary conditions for (2) are of Robin and Neumann type:

$$(s_w \boldsymbol{u}_t + \boldsymbol{K}\frac{\lambda_o\lambda_w}{\lambda_t}p_c'\nabla s_w)\cdot\boldsymbol{n} = s_{\text{in}}\boldsymbol{u}_t\cdot\boldsymbol{n}, \quad \text{on} \quad \Gamma_{s1}, \tag{5}$$

$$(-\boldsymbol{K}\frac{\lambda_o\lambda_w}{\lambda_t}p_c'\nabla s_w)\cdot\boldsymbol{n} = 0, \quad \text{on} \quad \Gamma_{s2}. \tag{6}$$

3 Scheme

In this section, we first establish some notation for the temporal and spatial discretization and we present our numerical scheme. Let $0 = t_0 < t^1 < \cdots < t^N = T$ be a subdivision of the time interval $(0, T)$. For any function v that depends on time and space, we introduce the notation $v^i = v(t^i, \cdot)$ for $i = 0, \ldots, N$. We also define the time step $\Delta t^i = t^{i+1} - t^i$.

The domain Ω is subdivided into triangular elements that form a mesh. Because of the refinements and derefinements, the mesh changes at every time step. Let us denote by $\mathcal{E}_h^i = \{E\}_E$ the mesh at time t^{i+1}. Let h^i be the maximum diameter of the elements. Let Γ_{h^i} be the union of the open sets that coincide with interior edges of elements of $\mathcal{E}_h^i$. Let e denote a segment of Γ_{h^i} shared by two triangles E^k and E^l of $\mathcal{E}_h^i$ $(k > l)$; we associate with e, once and for all, a unit normal vector $\boldsymbol{n}_e$ directed from E^k to E^l and we define formally the jump and average of a function ψ on e by:

$$[\psi] = (\psi|_{E^k})|_e - (\psi|_{E^l})|_e, \quad \{\psi\} = \frac{1}{2}(\psi|_{E^k})|_e + \frac{1}{2}(\psi|_{E^l})|_e.$$

If e is adjacent to $\partial\Omega$, then the jump and the average of ψ on e coincide with the trace of ψ on e and the normal vector $\boldsymbol{n}_e$ coincides with the outward normal $\boldsymbol{n}$.

For each integer r, we define a finite element subspace of discontinuous piecewise polynomials:

$$\mathcal{D}_r(\mathcal{E}_h^i) = \{v : v|_E \in P_r(E) \quad \forall E \in \mathcal{E}_h^i\},$$

where $P_r(E)$ is a discrete space containing the set of polynomials of total degree less than or equal to r on E. We will approximate the wetting phase pressure and saturation by discontinuous polynomials of order r_p and r_s respectively.

We now derive the variational formulation for the two-phase flow problem, by considering the pressure equation (1) and the saturation equation (2) separately.

3.1 The pressure equation

We rewrite (1) by defining $\boldsymbol{\chi} = -\boldsymbol{K}\lambda_o \nabla p_c = \boldsymbol{K}\lambda_o |p_c'| \nabla s_w$:

$$-\nabla \cdot (\boldsymbol{K}\lambda_t \nabla p_w) = -\nabla \cdot \boldsymbol{\chi}. \tag{7}$$

Multiplying (7) by a test function $v \in \mathcal{D}_{r_p}$, and using Green's formula on one element E yields:

$$\int_E \boldsymbol{K}\lambda_t \nabla p_w \cdot \nabla v - \int_{\partial E} (\boldsymbol{K}\lambda_t \nabla p_w \cdot \boldsymbol{n}_E) v = \int_E \boldsymbol{\chi} \cdot \nabla v - \int_{\partial E} (\boldsymbol{\chi} \cdot \boldsymbol{n}_E) v,$$

where $\boldsymbol{n}_E$ is the outward normal to E. Summing over all the elements in $\mathcal{E}_h^i$ and using the fact that p_w and $\boldsymbol{\chi}$ are smooth enough, namely $[p_w] = 0$, $[\boldsymbol{K}\lambda_t \nabla p_w \cdot \boldsymbol{n}_e] = 0$ and $[\boldsymbol{\chi} \cdot \boldsymbol{n}_e] = 0$, we have

$$\begin{aligned} &\sum_{E \in \mathcal{E}_h^i} \int_E \boldsymbol{K}\lambda_t \nabla p_w \cdot \nabla v - \sum_{e \in \Gamma_h^i \cup \partial\Omega} \int_e \{\boldsymbol{K}\lambda_t \nabla p_w \cdot \boldsymbol{n}_e\}[v] \\ &+ \sum_{e \in \Gamma_h^i} \int_e \{\boldsymbol{K}\lambda_t \nabla v \cdot \boldsymbol{n}_e\}[p_w] = \sum_{E \in \mathcal{E}_h^i} \int_E \boldsymbol{\chi} \cdot \nabla v - \sum_{e \in \Gamma_h \cup \partial\Omega} \int_e \boldsymbol{\chi} \cdot \boldsymbol{n}_e [v]. \end{aligned}$$

Making use of the boundary conditions (3) and (4), we obtain

$$\begin{aligned} &\sum_{E \in \mathcal{E}_h^i} \int_E \boldsymbol{K}\lambda_t \nabla p_w \cdot \nabla v - \sum_{e \in \Gamma_h^i \cup \Gamma_{p1}} \int_e \{\boldsymbol{K}\lambda_t \nabla p_w \cdot \boldsymbol{n}_e\}[v] \\ &\quad + \sum_{e \in \Gamma_h^i \cup \Gamma_{p1}} \int_e \{\boldsymbol{K}\lambda_t \nabla v \cdot \boldsymbol{n}_e\}[p_w] = \sum_{E \in \mathcal{E}_h^i} \int_E \boldsymbol{\chi} \cdot \nabla v \\ &\quad - \sum_{e \in \Gamma_h^i \cup \partial\Omega} \int_e \boldsymbol{\chi} \cdot \boldsymbol{n}_e [v] + \sum_{e \in \Gamma_{p1}} \int_e (\boldsymbol{K}\lambda_t \nabla v \cdot \boldsymbol{n}) p_{\text{dir}}. \end{aligned} \tag{8}$$

3.2 The saturation equation

Similarly, we define the auxiliary vector $\boldsymbol{\zeta} = \frac{\lambda_w}{\lambda_t}\boldsymbol{u}_t$. Then, (2) can be rewritten as:

$$\frac{\partial(\phi s_w)}{\partial t} - \nabla \cdot (\boldsymbol{K}\frac{\lambda_o \lambda_w}{\lambda_t} |p_c'| |\nabla s_w) = -\nabla \cdot \boldsymbol{\zeta}. \tag{9}$$

As for the pressure equation, we multiply by a test function $z \in \mathcal{D}_{r_s}$ over one element in $\mathcal{E}_h^i$, sum over all elements, and use the regularity of s_w and $\boldsymbol{\zeta}$. We

finally obtain after some algebraic manipulation:

$$\int_\Omega \frac{\partial(\phi s_w)}{\partial t} z + \sum_{E\in\mathcal{E}_h^i} \int_E \boldsymbol{K}\frac{\lambda_o\lambda_w}{\lambda_t}|p_c'|\nabla s_w\cdot\nabla z - \sum_{e\in\Gamma_h^i\cup\partial\Omega}\int_e \{\boldsymbol{K}\frac{\lambda_o\lambda_w}{\lambda_t}|p_c'|\nabla s_w\cdot\boldsymbol{n}_e\}[z]$$
$$+\sum_{e\in\Gamma_h^i}\int_e\{\boldsymbol{K}\frac{\lambda_o\lambda_w}{\lambda_t}|p_c'|\nabla z\cdot\boldsymbol{n}_e\}[s_w] = \sum_{E\in\mathcal{E}_h^i}\int_E \boldsymbol{\zeta}\cdot\nabla z - \sum_{e\in\Gamma_h^i\cup\partial\Omega}\int_e \boldsymbol{\zeta}\cdot\boldsymbol{n}_e[z].$$

Making use of the boundary conditions (5), (6) and the continuity of pressure, we have:

$$\begin{aligned}
&\int_\Omega \frac{\partial(\phi s_w)}{\partial t} z + \sum_{E\in\mathcal{E}_h^i} \int_E \boldsymbol{K}\frac{\lambda_o\lambda_w}{\lambda_t}|p_c'|\nabla s_w\cdot\nabla z - \sum_{e\in\Gamma_{s1}}\int_e s_w\boldsymbol{u}_t\cdot\boldsymbol{n}_e z\\
&-\sum_{e\in\Gamma_h^i}\int_e\{\boldsymbol{K}\frac{\lambda_o\lambda_w}{\lambda_t}|p_c'|\nabla s_w\cdot\boldsymbol{n}_e\}[z] + \sum_{e\in\Gamma_h^i}\int_e\{\boldsymbol{K}\frac{\lambda_o\lambda_w}{\lambda_t}|p_c'|\nabla z\cdot\boldsymbol{n}_e\}[s_w]\\
&\quad = \sum_{E\in\mathcal{E}_h^i}\int_E \boldsymbol{\zeta}\cdot\nabla z - \sum_{e\in\Gamma_h^i\cup\partial\Omega}\int_e \boldsymbol{\zeta}\cdot\boldsymbol{n}_e[z] - \sum_{e\in\Gamma_{s1}}\int_e s_{\text{in}}\boldsymbol{u}_t\cdot\boldsymbol{n}_e z\\
&-\sum_{e\in\Gamma_h^i}\int_e\frac{\lambda_w}{\lambda_t}\{\boldsymbol{K}\lambda_t\nabla z\cdot\boldsymbol{n}_e\}[p_w] - \sum_{\Gamma_{p1}}\int_e \boldsymbol{K}\lambda_w\nabla z\cdot\boldsymbol{n}_e(p_w-p_{\text{dir}}).
\end{aligned}\tag{10}$$

3.3 The discrete scheme

We discretize the time derivative by finite difference, which yields the backward Euler scheme. The initial approximations P_w^0, S_w^0 are simply obtained by a L^2 projection of the initial data $p_w(t=0)$ and $s_w(t=0)$. Based on (8) and (10), we formulate the following numerical method:
given $(P_w^i, S_w^i)\in\mathcal{D}_{r_p}\times\mathcal{D}_{r_s}$, find $(P_w^{i+1}, S_w^{i+1})\in\mathcal{D}_{r_p}\times\mathcal{D}_{r_s}$ such that for all $(v,z)\in\mathcal{D}_{r_p}\times\mathcal{D}_{r_s}$:

$$\begin{aligned}
&\sum_{E\in\mathcal{E}_h^i}\int_E \boldsymbol{K}\lambda_t(S_w^i)\nabla P_w^{i+1}\cdot\nabla v - \sum_{e\in\Gamma_h^i\cup\Gamma_{p1}}\int_e\{\boldsymbol{K}\lambda_t(S_w^i)\nabla P_w^{i+1}\cdot\boldsymbol{n}_e\}[v]\\
&\quad+\sum_{e\in\Gamma_h^i\cup\Gamma_{p1}}\int_e\{\boldsymbol{K}\lambda_t(S_w^i)\nabla v\cdot\boldsymbol{n}_e\}[P_w^{i+1}] = \sum_{E\in\mathcal{E}_h^i}\int_E\boldsymbol{\chi}_h^i\cdot\nabla v\\
&\quad-\sum_{e\in\Gamma_h^i\cup\partial\Omega}\int_e\boldsymbol{\chi}_h^{i\uparrow}\cdot\boldsymbol{n}_e[v] + \sum_{e\in\Gamma_{p1}}\int_e(\boldsymbol{K}\lambda_t(S_w^i)\nabla v\cdot\boldsymbol{n})p_{\text{dir}},
\end{aligned}\tag{11}$$

and

$$\int_\Omega \frac{\phi}{\Delta t^i} S_w^{i+1} z + \sum_{E\in\mathcal{E}_h^i} \int_E \boldsymbol{K} \frac{\lambda_o(S_w^i)\lambda_w(S_w^i)}{\lambda_t(S_w^i)} |p_c'(S_w^i)| \nabla S_w^{i+1} \cdot \nabla z$$

$$- \sum_{e\in\Gamma_{s1}} \int_e S_w^{i+1} \boldsymbol{U}_t^i \cdot \boldsymbol{n}_e z - \sum_{e\in\Gamma_h^i} \int_e \{\boldsymbol{K} \frac{\lambda_o(S_w^i)\lambda_w(S_w^i)}{\lambda_t(S_w^i)} |p_c'(S_w^i)| \nabla S_w^{i+1} \cdot \boldsymbol{n}_e\}[z]$$

$$+ \sum_{e\in\Gamma_h^i} \int_e \{\boldsymbol{K} \frac{\lambda_o(S_w^i)\lambda_w(S_w^i)}{\lambda_t(S_w^i)} |p_c'(S_w^i)| \nabla z \cdot \boldsymbol{n}_e\}[S_w^{i+1}]$$

$$= \int_\Omega \frac{\phi}{\Delta t^i} S_w^i z + \sum_{E\in\mathcal{E}_h^i} \int_E \boldsymbol{\zeta}_h^i \cdot \nabla z - \sum_{e\in\Gamma_h^i\cup\Gamma_{p1}} \int_e \boldsymbol{\zeta}_h^{i\uparrow} \cdot \boldsymbol{n}_e [z] - \sum_{e\in\Gamma_{s1}} \int_e s_{\text{in}} \boldsymbol{U}_t^i \cdot \boldsymbol{n}_e$$

$$- \sum_{e\in\Gamma_h^i} \int_e \frac{\lambda_w(S_w^i)}{\lambda_t(S_w^i)} \{\boldsymbol{K}\lambda_t(S_w^i) \nabla z \cdot \boldsymbol{n}_e\}[P_w^i] - \sum_{e\in\Gamma_{p1}} \int_e \boldsymbol{K}\lambda_w(S_w^i) \nabla z \cdot \boldsymbol{n}_e (P_w^i - p_{\text{dir}}), \tag{12}$$

where $\boldsymbol{U}_t^i, \boldsymbol{\zeta}_h^i$ and $\boldsymbol{\chi}_h^i$ are the approximates of $\boldsymbol{u}_t^i, \boldsymbol{\zeta}^i$ and $\boldsymbol{\chi}^i$.

$$\boldsymbol{U}_t^i = -\boldsymbol{K}\lambda_w(S_w^i)\nabla P_w^i - \boldsymbol{K}\lambda_o(S_w^i)(p_c'(S_w^i)\nabla S_w^i + \nabla P_w^i)$$
$$\boldsymbol{\chi}_h^i = \boldsymbol{K}\lambda_o(S_w^i)|p_c'(S_w^i)|\nabla S_w^i$$
$$\boldsymbol{\zeta}_h^i = \frac{\lambda_w(S_w^i)}{\lambda_t(S_w^i)}\{\boldsymbol{U}_t^i\}.$$

Because of the discontinuous approximations, there are two values for the functions $\boldsymbol{\chi}^i$ and $\boldsymbol{\zeta}^i$ on an interior edge. These quantities are then replaced by the upwind numerical fluxes $\boldsymbol{\chi}_h^{i\uparrow}$ and $\boldsymbol{\zeta}_h^{i\uparrow}$. Upwinding is done with respect to the normal component of the average of the total velocity $\boldsymbol{U}_t$

$$\forall e = \partial E^k \cap \partial E^l, \quad (k > l), \quad \forall \psi, \quad \psi^\uparrow = \begin{cases} \psi|_{E^k} \text{ if } \{\boldsymbol{U}_t^i\} \cdot \boldsymbol{n}_e \geq 0, \\ \psi|_{E^l} \text{ if } \{\boldsymbol{U}_t^i\} \cdot \boldsymbol{n}_e < 0. \end{cases}$$

From the derivations in Sections 3.1 and 3.2, we obtain the consistency of the NIPG scheme.

Lemma 1 *If (p_w, s_w) is a solution of (1), (2), then (p_w, s_w) is also a solution of (11), (12).*

3.4 Local Mass Balance

Let us fix an element E and a test function $v \in \mathcal{D}_{r_p}$ that vanishes outside of E. For simplicity, we assume that E is an interior element in Ω. The pressure

equation (11) becomes:

$$\int_E \boldsymbol{K}\lambda_t(S_w^i)\nabla P_w^{i+1}\cdot\nabla v - \int_{\partial E}\{\boldsymbol{K}\lambda_t(S_w^i)\nabla P_w^{i+1}\cdot\boldsymbol{n}_E\}v$$
$$+\int_{\partial E}\frac{1}{2}\boldsymbol{K}\lambda_t(S_w^i)\nabla v\cdot\boldsymbol{n}_E[P_w^{i+1}] = \int_E \boldsymbol{\chi}_h^i\cdot\nabla v - \int_{\partial E}\boldsymbol{\chi}_h^{i\uparrow}\cdot\boldsymbol{n}_E v.$$

If in addition, we let v to be equal to one over E, we obtain the local mass property satisfied by the approximations:

$$-\int_{\partial E}\{\boldsymbol{K}\lambda_t(S_w^i)\nabla P_w^{i+1}\cdot\boldsymbol{n}_E\}v - \int_{\partial E}\boldsymbol{\chi}_h^{i\uparrow}\cdot\boldsymbol{n}_E v = 0.$$

3.5 Slope Limiting

Approximations of high order yield overshoot and undershoot in the neighborhood of the front of the injected phase. Slope limiters are the appropriate tools for decreasing the local oscillations [5,9]. To our knowledge there is no analysis available for slope limiters in 2D and 3D, even on a conforming mesh. We are also not aware of limiters that would handle nonconforming meshes. In this section, we propose a limiting technique that can handle meshes with hanging nodes. This procedure is successfully tested for our two-phase flow problem. We apply the limiting technique to the approximations P_w^{i+1} and S_w^{i+1} after each time step t^{i+1}.

In what follows, we say that one element E is active if it belongs to the mesh $\mathcal{E}_h^i$, i.e., if it is used in the computation of (11), (12). The element can become inactive if it is refined and thus its children are created and activated. The limiting process consists of two steps.
First, we loop through all the active elements starting from the oldest generation to the youngest (in general this would mean that the order is in decreasing size). For example, Fig. 1 shows an example of five elements of different generation: if G denotes the generation of the elements E_0 and E_1, then elements E_3 and E_4 are of younger generation $G+1$ and element E_2 is of older generation $G-1$. Thus, it is assumed that the limiting process has been already applied to E_2.
1) *Neighbor averages*: We first compute the average saturation for the element to be limited and all neighboring elements as follows. Let $\bar{S}_0$ denote the average saturation over E_0 and let $\bar{S}_j$ denote a function associated to each side $j\in\{1,2,3\}$ of E_0. For E_0 and the neighbors of the same generation, we have the usual averaging operator:

$$\bar{S}_0 = \mathcal{A}(E_0),\quad \bar{S}_1 = \mathcal{A}(E_1),\quad \text{where}\quad \mathcal{A}(E) = \frac{1}{|E|}\int_E S_w^{i+1}.$$

To compute $\bar{S}_2$ corresponding to the side 2 of E_0 and the element E_2 that is

of older generation, we first locate the barycenter b_2 of an imaginary child $\tilde{C}_2$ of the same generation of E_0 (see dashed lines in Fig. 1). We then set

$$\bar{S}_2 = S_w^{i+1}|_{E_2}(b_2)$$

We note that $\bar{S}_2 = \mathcal{A}(\tilde{C}_2)$. The smaller elements E_3 and E_4 belong to a parent $\tilde{E}$ (see dotted lines in Fig. 1). If we denote by $F_1^{\tilde{E}}, \ldots, F_4^{\tilde{E}}$ the children of $\tilde{E}$, we can write

$$\bar{S}_3 = \frac{1}{4} \sum_{l=1}^{4} \mathcal{B}(F_l^{\tilde{E}}),$$

where the function $\mathcal{B}$ is defined recursively as (using the notation F_l^E for the l^{th} child of E):

$$\mathcal{B}(E) = \begin{cases} \frac{1}{|E|} \int_E S_w^i, & \text{if} \quad E \quad \text{active}, \\ \frac{1}{4} \sum_{l=1}^{4} \mathcal{B}(F_l^E), & \text{otherwise}. \end{cases}$$

If the edge j is a boundary edge, then $\bar{S}_j$ is defined according to the boundary conditions.

$$\bar{S}_j = s_{\text{in}} \quad \text{on} \quad \Gamma_{s1}, \quad \bar{S}_j = \bar{S}_0 \quad \text{on} \quad \Gamma_{s2}.$$

2) *Test:* We then compute the saturation $S_w^{i+1}|_{E_0}(m_j)$ evaluated at the midpoint m_j of each edge j and we check that this value is between $\bar{S}_j$ and $\bar{S}_0$. We stop here if the test is successful, otherwise we continue to step 3.
3) *Construction of three linears:* Based on the technique by Durlofsky et al [6], we construct three linears using the points b_j and the averages $\bar{S}_j$. For instance, if we write the linears as $\mathcal{L}_j(x, y) = a_0^j + a_1^j x + a_2^j y$, for $j \in \{1, 2, 3\}$, they are uniquely determined by

$$\mathcal{L}_j(b_0) = \bar{S}_0 \text{ and } \mathcal{L}_j(b_l) = \bar{S}_l, \text{ for } l \neq j.$$

We then rank the linears by decreasing $\sqrt{(a_1^j)^2 + (a_2^j)^2}$ and check that for the values of the linears evaluated at the midpoint m_l, $\mathcal{L}_j(m_l)$, is between $\bar{S}_l$ and $\bar{S}_0$ for $1 \geq l \geq 3$. If none of the constructed linears satisfy the test then the slope is reduced to 0.

Second, we loop through all elements and check that their slopes are not too large in the euclidean norm. If it is larger than a cut-off value (set up by user), we scale it by the ratio cut-off/norm.

4 Adaptivity strategy

In this section, we define the error indicators and present the adaptivity in space and time techniques.

The error indicators are based on a posteriori error estimates obtained for linear parabolic problems [8] We define the following quantities:

$$R_{\text{vol}} = -\frac{\phi}{\Delta t^i}(S_w^{i+1} - S_w^i) + \nabla \cdot \left(\boldsymbol{K} \frac{\lambda_n(S_w^i)\lambda_w(S_w^i)}{\lambda_t(S_w^i)} |p_c'(S_w^i)| \nabla S_w^i \right) - \nabla \cdot \left(\frac{\lambda_w(S_w^i)}{\lambda_t(S_w^i)} \boldsymbol{U}_t^i \right)$$

$$R_{\text{e1}} = [S_w^{i+1}],$$

$$R_{\text{e2}} = [\boldsymbol{K} \frac{\lambda_w(S_w^i)\lambda_n(S_w^i)}{\lambda_t(S_w^i)} |p_c'(S_w^i)| \nabla S_w^{i+1} \cdot \boldsymbol{n}] + \{\boldsymbol{U}_t^i\} \cdot \boldsymbol{n} [S_w^{i+1}],$$

$$R_{\text{es1}} = s_{\text{in}} \boldsymbol{U}_t^i \cdot \boldsymbol{n} - S_w^{i+1} \boldsymbol{U}_t^i \cdot \boldsymbol{n} + \boldsymbol{K} \frac{\lambda_n(S_w^i)\lambda_w(S_w^i)}{\lambda_t(S_w^i)} |p_c'(S_w^i)| \nabla S_w^{i+1} \cdot \boldsymbol{n},$$

$$R_{\text{es2}} = \boldsymbol{K} \frac{\lambda_n(S_w^i)\lambda_w(S_w^i)}{\lambda_t(S_w^i)} |p_c'(S_w^i)| \nabla S_w^{i+1} \cdot \boldsymbol{n}.$$

Then the error indicator η_E computed on each element E is

$$\eta_E = \Big(h_E^4 \|R_{\text{vol}}\|_{0,E}^2 + \sum_{e \in \partial E \setminus \partial\Omega} (h_e^3 \|R_{\text{e2}}\|_{0,e}^2 + (h_e + 1)\|R_{\text{e1}}\|_{0,e}^2) + \sum_{e \in \partial E \cap \Gamma_{s1}} h_e^3 \|R_{\text{es1}}\|_{0,e}^2 + \sum_{e \in \partial E \cap \Gamma_{s2}} h_e^3 \|R_{\text{es2}}\|_{0,e}^2 \Big)^{1/2},$$

where h_E is the diameter of the element E and $h_e = \max(h_{E_k}, h_{E_l})$ if the edge e is shared by elements E_k and E_l. Note that the notation $\partial E \setminus \partial\Omega$ means that the edges are interior edges only.

4.2 Adaptive mesh refinement technique

Let us assume that the solution P_w^i and S_w^i have been obtained at the i^{th} time step. We compute the error indicator η_E for each active element E. Then, we first refine the appropriate elements and second apply the derefinement technique.

Refinement: We refine each element whose error indicator is greater than a threshold value η_R. Note that this threshold value can be a percentage of the maximum of the error indicators. Fig. 2 show how one element (also called parent) is refined into four smaller elements (also called children).

Derefinement: We consider a parent element for derefinement if (A) all of its children are active, (B) the error indicator of each of its children is less than a threshold value η_D, and (C) the element was not refined during the current time step. For each parent element meeting these requirements, an L^2 projection is performed to retrieve the degrees of freedom of the parent. Before

actually doing the derefinement, we check that the parent error indicator is less than η_R. If it is, we then derefine. If it is not, we do not derefine.

4.3 Adaptive time stepping technique

For time strategy, we allow the time step to vary during the simulation. We uniformly divide the simulation interval $(0, T)$ into *whole steps* of length Δt^i. At the start of each whole step, we try to compute the saturation for time $t^i + \Delta t^i$, where t^i is the current time. If the resulting saturation function is satisfactory, then we record it, calculate the new pressure function, and proceed to the next whole step.
On the other hand, if the resulting saturation function is unsatisfactory, then we discard it and subdivide the whole step into two *half steps*. We then compute the saturation for the time at which the first half step ends. If the result is acceptable, we proceed to the second half step, and if its result is also acceptable, then we continue on to the next whole step. If one of the half steps does not yield satisfactory results, then we divide it into quarter steps, proceeding in the same manner as before, with the exception that we accept the results of the quarter steps regardless of how satisfactory they are. For the numerical simulations in this paper, a resulting saturation function was deemed unsatisfactory if the average saturation in any element exceeded the physically permissible range by more than 0.01; otherwise, it was considered satisfactory.
The main purpose of this time stepping technique is to speed up computation without losing accuracy, thus to increase the efficiency of the method.

5 Numerical examples

In the following simulations, we assume that the fluid and medium properties are:

$$\mu_o = 0.002\,\mathrm{kg/(ms)}, \quad \mu_w = 0.0005\,\mathrm{kg/(ms)}, \quad \phi = 0.2,$$
$$s_w(t=0) = 0.2, \quad p_w(t=0) = 3.45 \times 10^{-6}\mathrm{Pa},$$
$$s_{in} = 0.95, \quad s_{rw} = 0.15, \quad s_{ro} = 0,$$
$$p_d = 5 \times 10^3\mathrm{Pa}.$$

The orders of approximation are discontinuous piecewise linears for the saturation and discontinuous piecewise quadratics for the pressure. For the adaptive refinements and derefinements, we chose $\eta_R = 1 \times 10^{-1}$ and $\eta_D = (1/3)\eta_R$. The well-known five-spot problem on homogeneous and heterogeneous media is first considered, then simulations with highly varying permeability are

presented.

5.1 Five-spot on homogeneous medium

The permeability tensor is $\boldsymbol{K} = 10^{-11}\mathbf{I}\mathrm{m}^2$, where $\mathbf{I}$ is the identity matrix. Fig. 3 shows the coarse mesh and the domain Ω embedded into the square $(-300, 300)^2$. Four injection wells are located at each corner of the domain; the well bore corresponds to the boundary Γ_{s1} and part of Γ_{p1}, where we assume that $p_{\mathrm{dir}} = 3.45 \times 10^6\mathrm{Pa}$. A production well is located in the interior of the domain; the well bore corresponds to the remainder of Γ_{p1} and the pressure is set $p_{\mathrm{dir}} = 2.41 \times 10^6\mathrm{Pa}$. The flow of the phases is thus driven by the gradient of pressure from the injection wells to the production wells.

The simulation is run for 52.5 days with a time step varying between 0.001875 days and 0.0075 days. Three dimensional views of contours of wetting phase pressure and saturation at selected times are shown in Fig.4 and Fig. 5.

In order to better analyze this example and because of the symmetry of the problem, we re-run the simulations on one quarter of the domain; this yields the quarter-five spot problem shown in Fig. 6. The injection well is at the left bottom corner whereas the production well is at the right top corner. The domain is now embedded into $(0, 300)^2$.

The contours of wetting phase pressure and saturation at selected times are shown in Fig.7 and Fig. 8. The locally refined and derefined meshes are also given on these figures. One can conclude that the proposed error indicators capture well the location of the front. As expected, the mesh is more refined in the neighborhood of the saturation front. It also appears that the mesh stays refined at the neighborhood of the injection well bore.

We compare the adaptive results with those obtained on the coarse mesh refined uniformly three times. The pressure and saturation contours are given in Fig. 9 and Fig. 10. Here, the time step varies between 0.015 days and 0.00375 days. The contours are similar to the adaptive ones. For better comparison, we show the pressure and saturation profiles along the diagonal $\{(x, y) : x = y\}$ (see Fig. 11). Using adaptive refinement and derefinement decreases significantly the cost of the computation, as shown in Table 1. The columns for AMR correspond to adatively refined meshes, and the columns for UNI correspond to uniformly refined meshes.

5.2 Five spot on heterogeneous medium

This simulation is identical to the one above except for the permeability tensor. Here, $\boldsymbol{K}$ is discontinuous and is equal to $10^{-13}\mathrm{m}^2\mathbf{I}$ in a small subdomain. In the rest of domain, $\boldsymbol{K} = 10^{-11}\mathbf{I}\mathrm{m}^2$. We present the contours of the pressure and saturation at different times in Fig. 12 and Fig 13. Clearly, the region of low permeability is not invaded by the injected wetting phase. This shows that the scheme has very little numerical diffusion.

5.3 Highly varying permeability field

We consider a square domain $(0, 400)^2$ with varying permeability as shown in Fig. 14. The permeability is $10^{-11}\mathbf{I}\mathrm{m}^2$ except in several small regions where it is 10^5 times smaller (see [10]). The simulation is run for 70 days. The time step varies between 2.1875×10^{-3} days and 8.75×10^{-3} days. The vertical boundaries correspond to Γ_{p1} where the same pressure p_{dir} as in the previous examples is imposed. The left vertical boundary corresponds to Γ_{s1}. Saturation contours on adaptively refined meshes are shown in Fig. 15. The degrees of freedom are $8232, 13281, 17070$ and 19131 for the respective times $17.5, 35, 52.5$ and 70 days. The figures show clearly that there is very little numerical diffusion. For comparison, we show the contours obtained on a uniform mesh, which corresponds to 38400 degrees of freedom (see Fig. 16). The coarse mesh has been refined twice, and this produces a computational time of 24 hours on a single processor. For another level of refinement, the simulation would run for one week.

6 Conclusions

This paper present adaptivity techniques in space and time. We show that the adaptive simulations are more efficient than the simulations obtained on uniform meshes and with constant time step. The proposed DG scheme yields very little numerical diffusion. Finally, we define new slope limiters that are robust on nonconforming meshes.

References

[1] P. Bastian. High order discontinuous Galerkin methods for flow and transport in porous media. *Challenges in Scientific Computing CISC 2002*, 35, 2003.

[2] P. Bastian. Discontinuous Galerkin methods for two-phase flow in porous media. *submitted*, 2004. Also technical report, 2004-28, , IWR (SFB 359), Heidelberg University.

[3] B.Rivière. Numerical study of a discontinuous Galerkin method for incompressible two-phase flow. In *Proceedings of ECCOMAS*, 2004.

[4] R.H. Brooks and A.T. Corey. Hydraulic properties of porous media. *Hydrol. Pap.*, 3, 1964.

[5] B. Cockburn and C.-W. Shu. TVB Runge-Kutta local projection discontinuous Galerkin finite element method for conservative laws II: general framework. *Mathematics of Computation*, 52:411–435, 1989.

[6] L.J. Durlofsky, B. Engquist, and S. Osher. Triangle based adaptive stencils for the solution of hyperbolic conservation laws. *Journal of Computational Physics*, 98:64–73, 1992.

[7] Y. Epshteyn and B. Rivière. Fully implicit discontinuous Galerkin schemes for multiphase flow. Technical Report TR-MATH 05-07, University of Pittsburgh, 2005. submitted.

[8] A. Ern and J. Proft. A posteriori discontinuous Galerkin error estimates for transient convection-diffusion equations. *Applied Mathematics Letters*, 18(7):833–841, 2005.

[9] H.Hoteit, Ph.Ackerer, R.Mosé, J.Erhel, and B.Philippe. New two-dimensional slope limiters for discontinuous Galerkin methods on arbitrary meshes. *International J. Numer. Meth. Engng*, 61:2566–2593, 2004.

[10] L.J.Durlofsky. Accuracy of mixed and control volume finite element approximations to darcy velocity and related quantities. *Water Resources Research*, 30(4):965–973, 1994.

[11] D. Nayagum, G. Schäfer, and R. Mosé. Modelling two-phase incompressible flow in porous media using mixed hybrid and discontinuous finite elements. *Computational Geosciences*, 8(1):49–73, 2004.

[12] B. Rivière and E. Jenkins. In pursuit of better models and simulations, oil industry looks to the math sciences. *SIAM News*, Jan/Feb, 2002.

[13] B. Rivière and M.F. Wheeler. Discontinuous Galerkin methods for flow and transport problems in porous media. *Communications in Numerical Methods in Engineering*, 18:63–68, 2002.

[14] B. Rivière and M.F. Wheeler. Non conforming methods for transport with nonlinear reaction. *Proceedings of an AMS-IMS-SIAM Joint Summer Research Conference on Fluid Flow and Transport in Porous Media: Mathematical and Numerical Treatment*, 2002.

[15] S. Sun and M.F. Wheeler. Symmetric and non-symmetric discontinuous Galerkin methods for reactive transport in porous media. *SIAM Journal on Numerical Analysis*, 43(1):195–219, 2005.

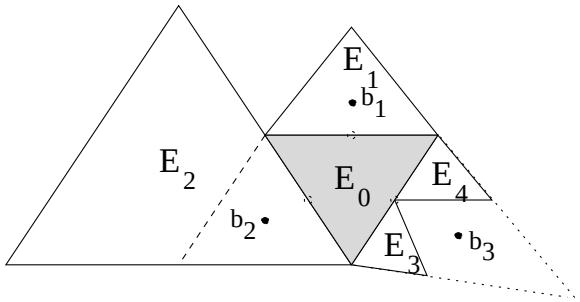

Fig. 1. Slope limiting on non-conforming meshes.

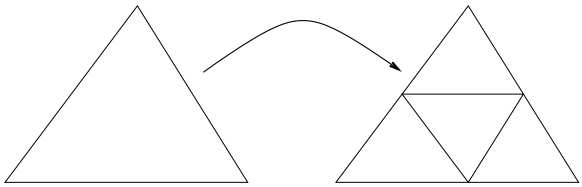

Fig. 2. Refinement of a triangular element.

Table 1
Number of degrees of freedom for adaptive and non-adaptive simulations.

	DOFS press		DOFS sat	
t (days)	AMR	UNI	AMR	UNI
7.5	2538	25344	1269	12672
15	2412	25344	1206	12672
22.5	2142	25344	1071	12672
30	2466	25344	1233	12672

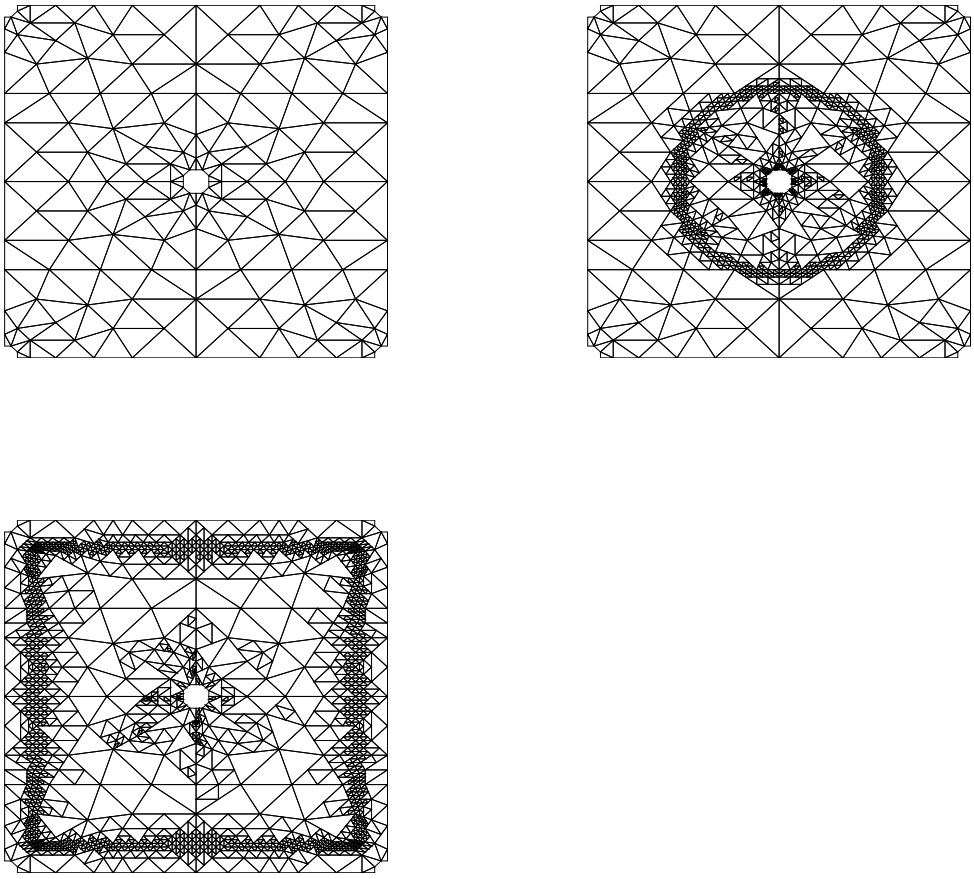

Fig. 3. Five-well example: coarse mesh at initial time and adaptive meshes obtained at 15 and 45 days.

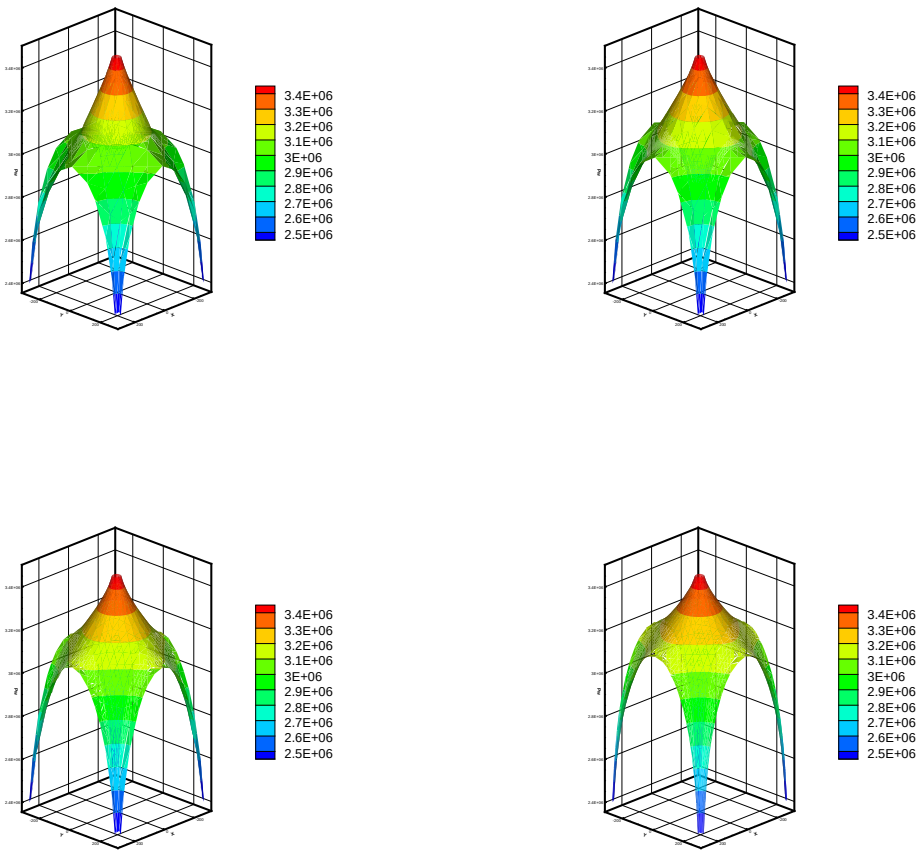

Fig. 4. Five-well example: three-dimensional pressure contours at 15, 30, 45 and 52.5 days.

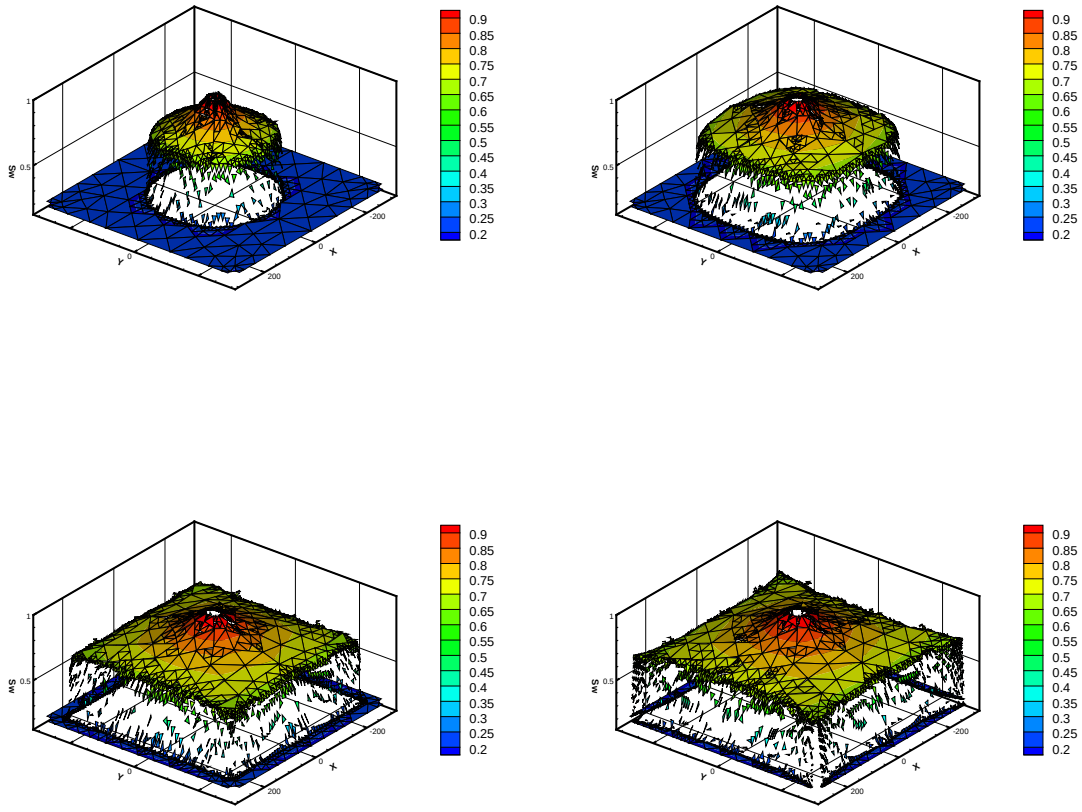

Fig. 5. Five-well example: three-dimensional saturation contours at 15, 30, 45 and 52.5 days.

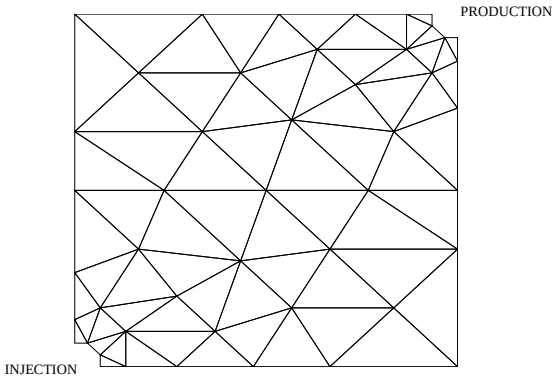

Fig. 6. Domain and coarse mesh for quarter-five spot.

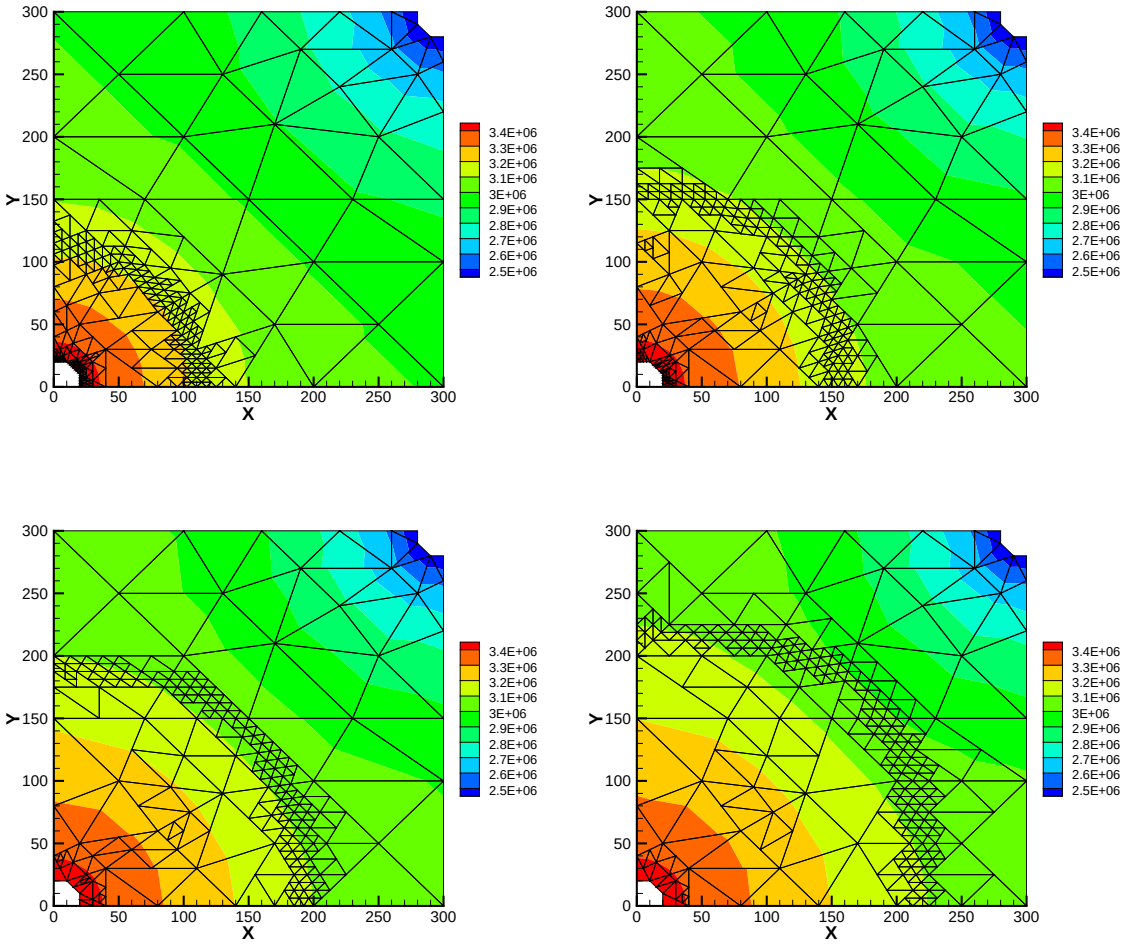

Fig. 7. Two-dimensional pressure contours at 7.5, 15, 22.5 and 30 days.

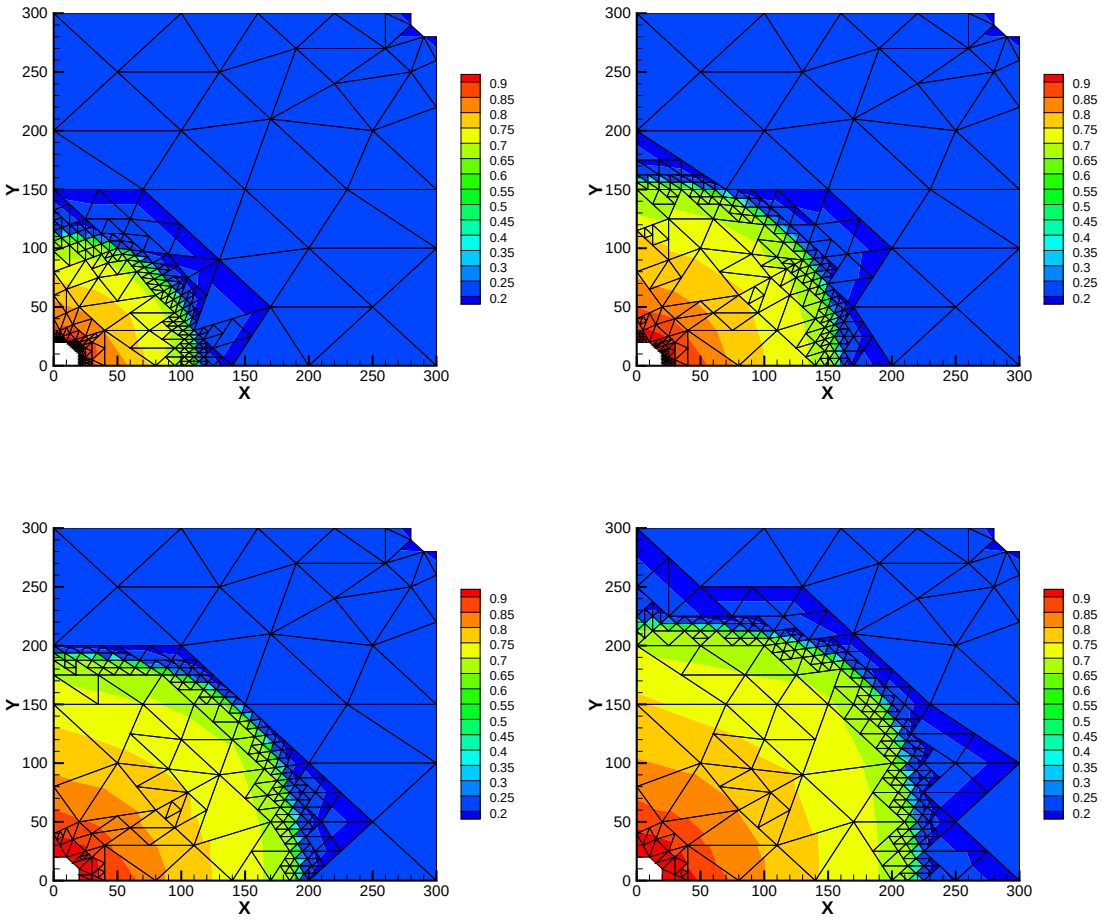

Fig. 8. Two-dimensional saturation contours at 7.5, 15, 22.5 and 30 days.

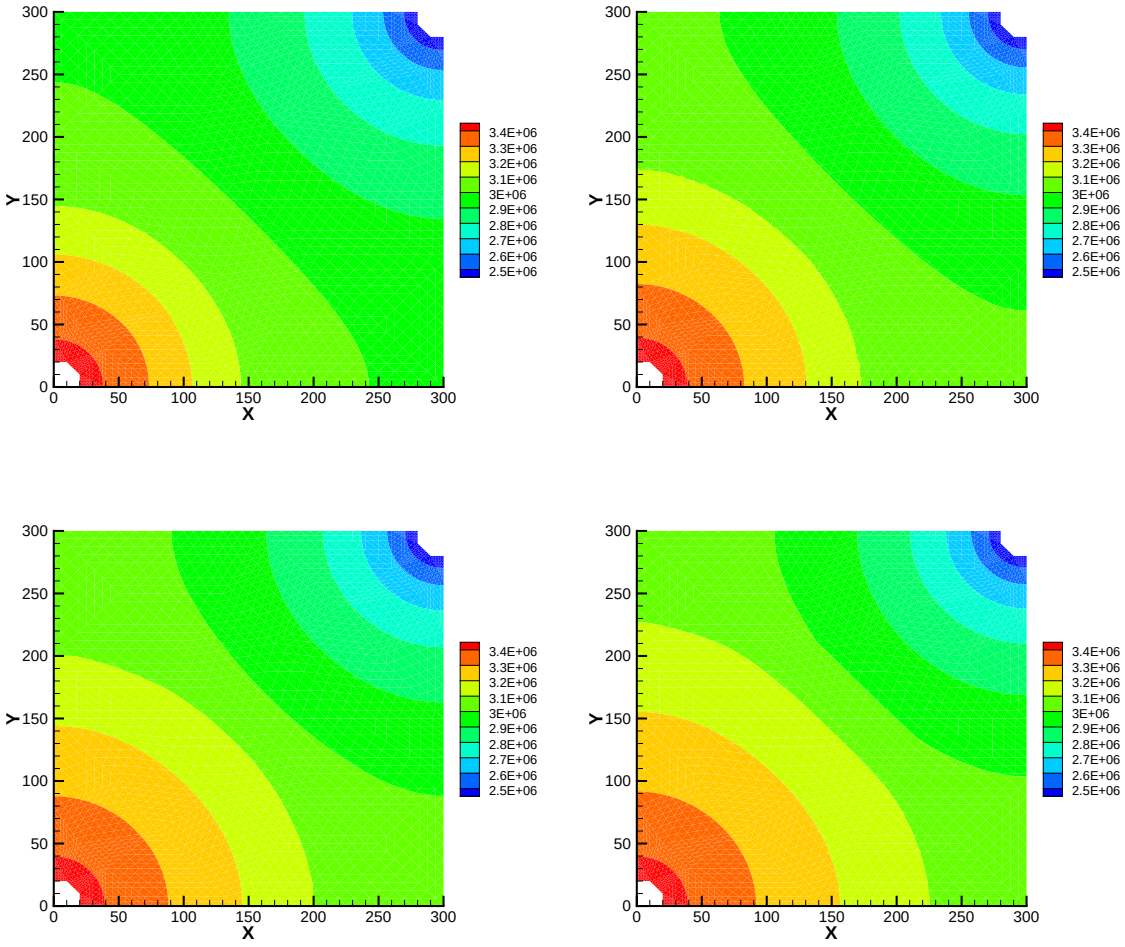

Fig. 9. Two-dimensional pressure contours at 7.5, 15, 22.5 and 30 days obtained on uniformly refined meshes.

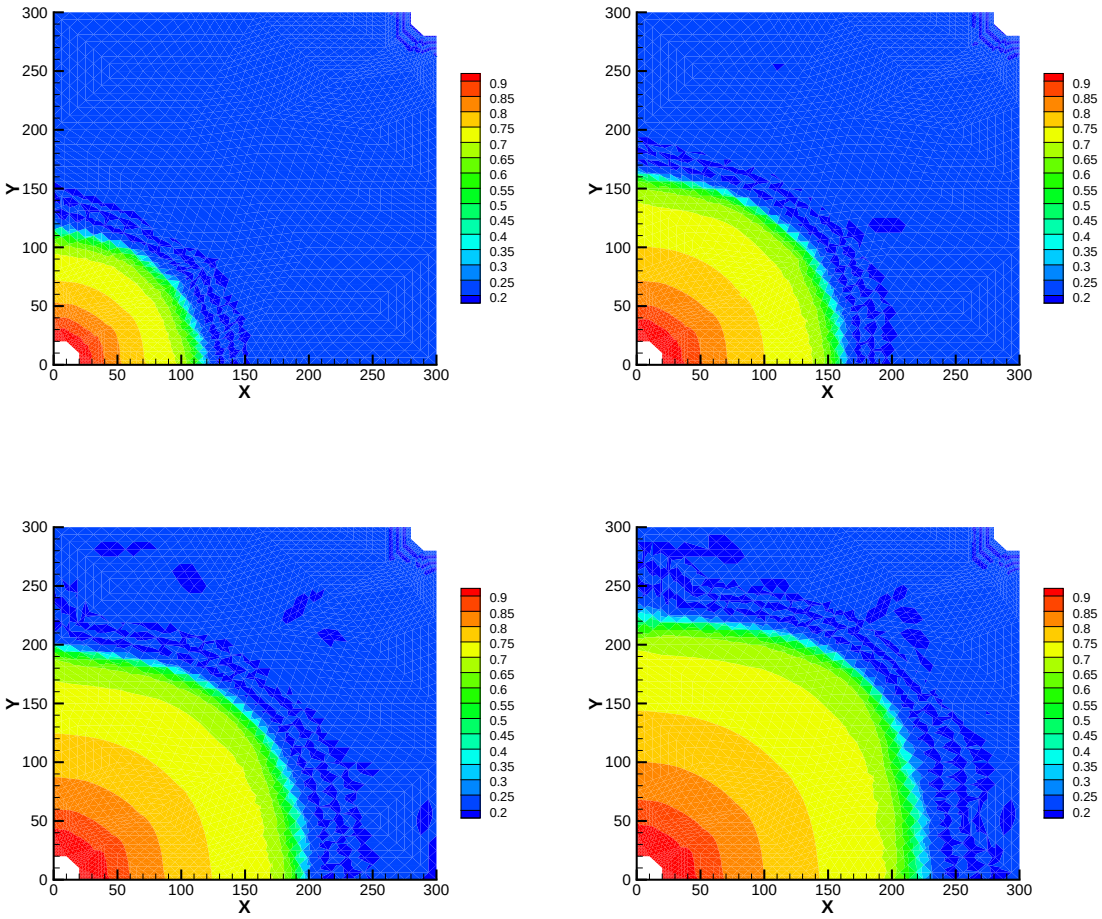

Fig. 10. Two-dimensional saturation contours at 7.5, 15, 22.5 and 30 days obtained on uniformly refined meshes.

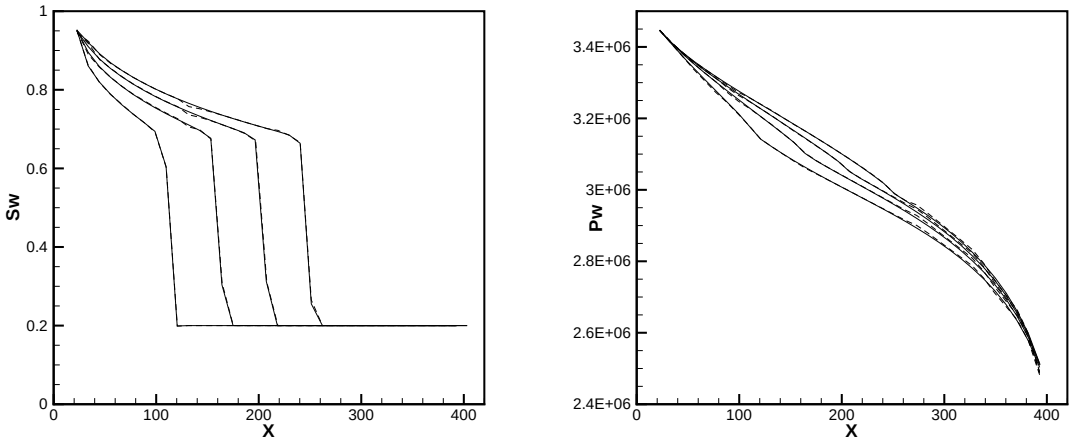

Fig. 11. Saturation (left) and pressure (right) fronts along the diagonal line $x = y$ at 7.5, 15, 22.5 and 30 days. The solid line corresponds to a uniform mesh refinement (h3) and the dashed line to an adaptively refined mesh

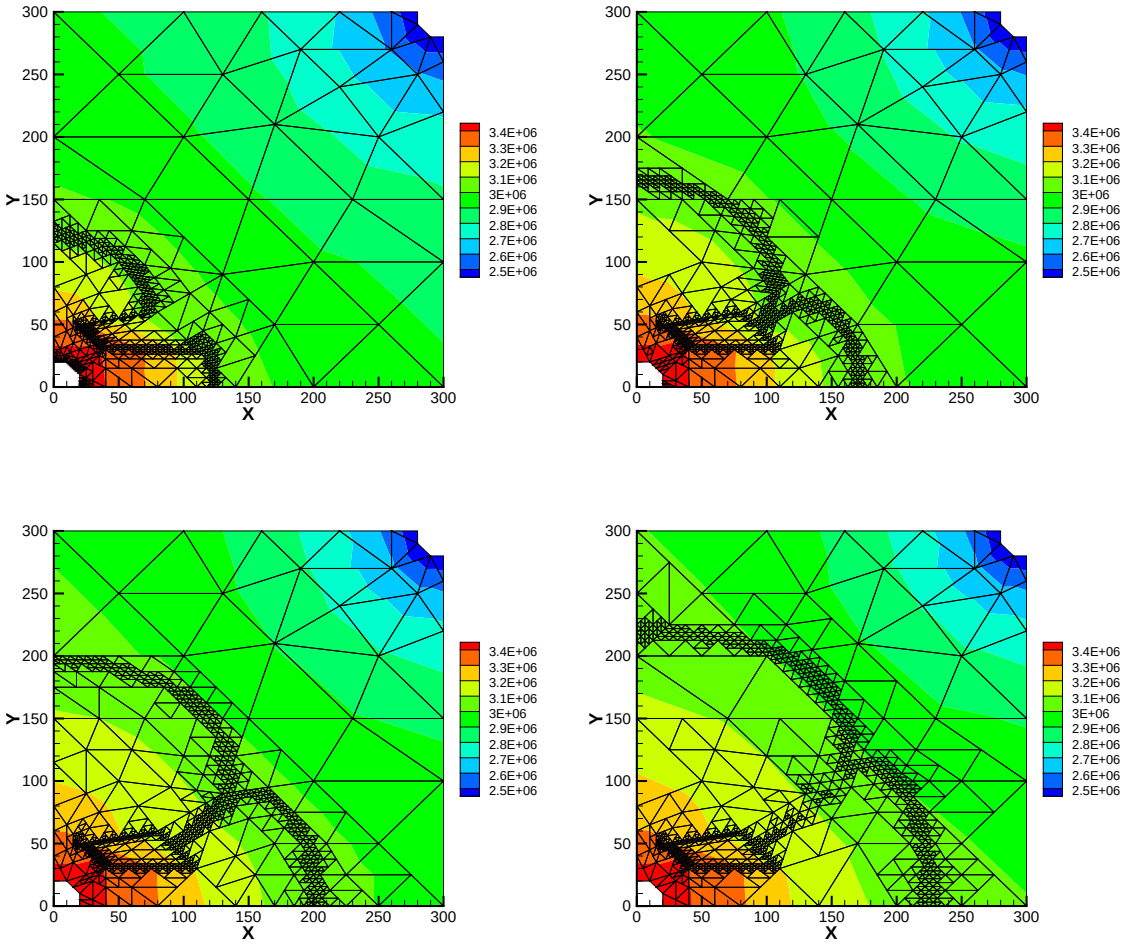

Fig. 12. Two-dimensional pressure contours at 7.5, 15, 22.5 and 30 days on an inhomogeneous medium.

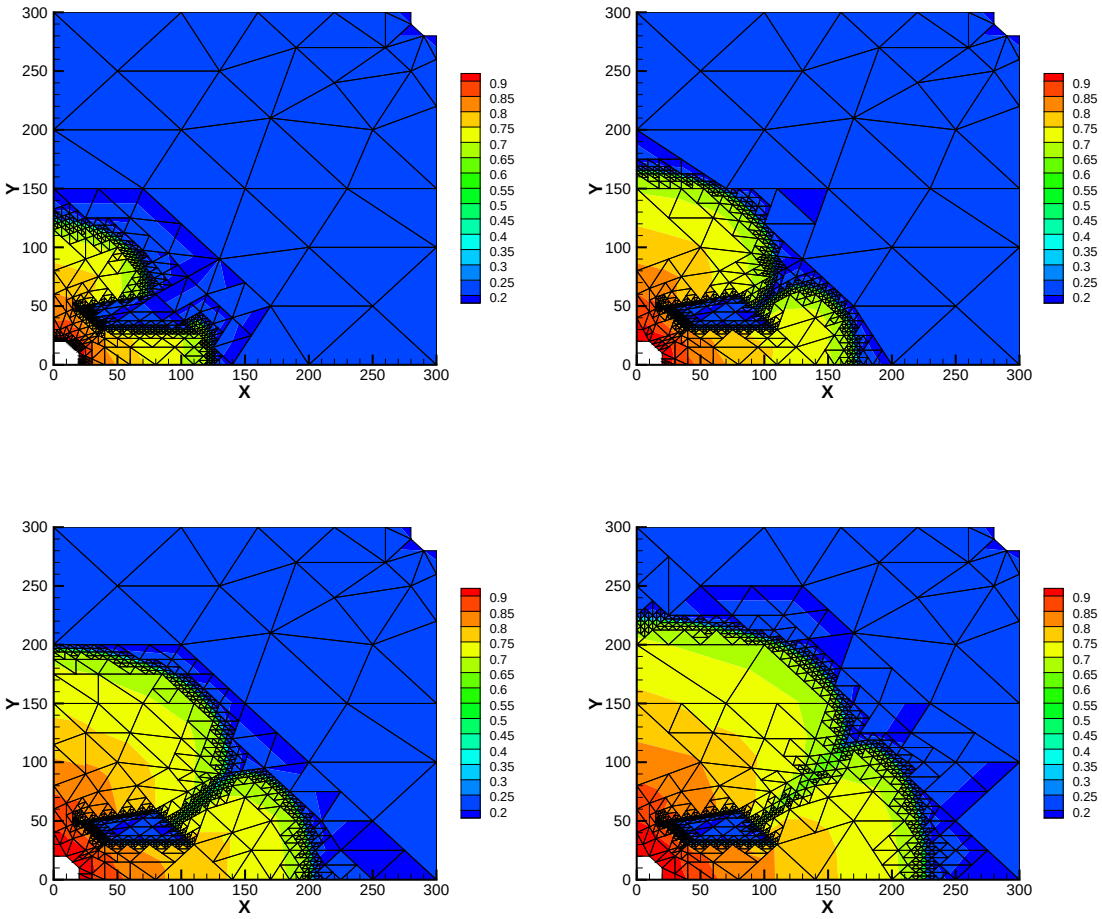

Fig. 13. Two-dimensional saturation contours at 7.5, 15, 22.5 and 30 days on an inhomogeneous medium.

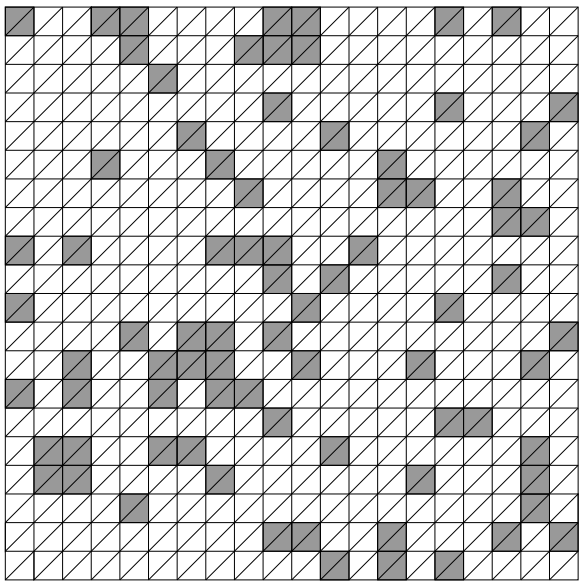

Fig. 14. Permeability field and coarse mesh: permeability is 10^{-11} in white regions and 10^{-16} elsewhere.

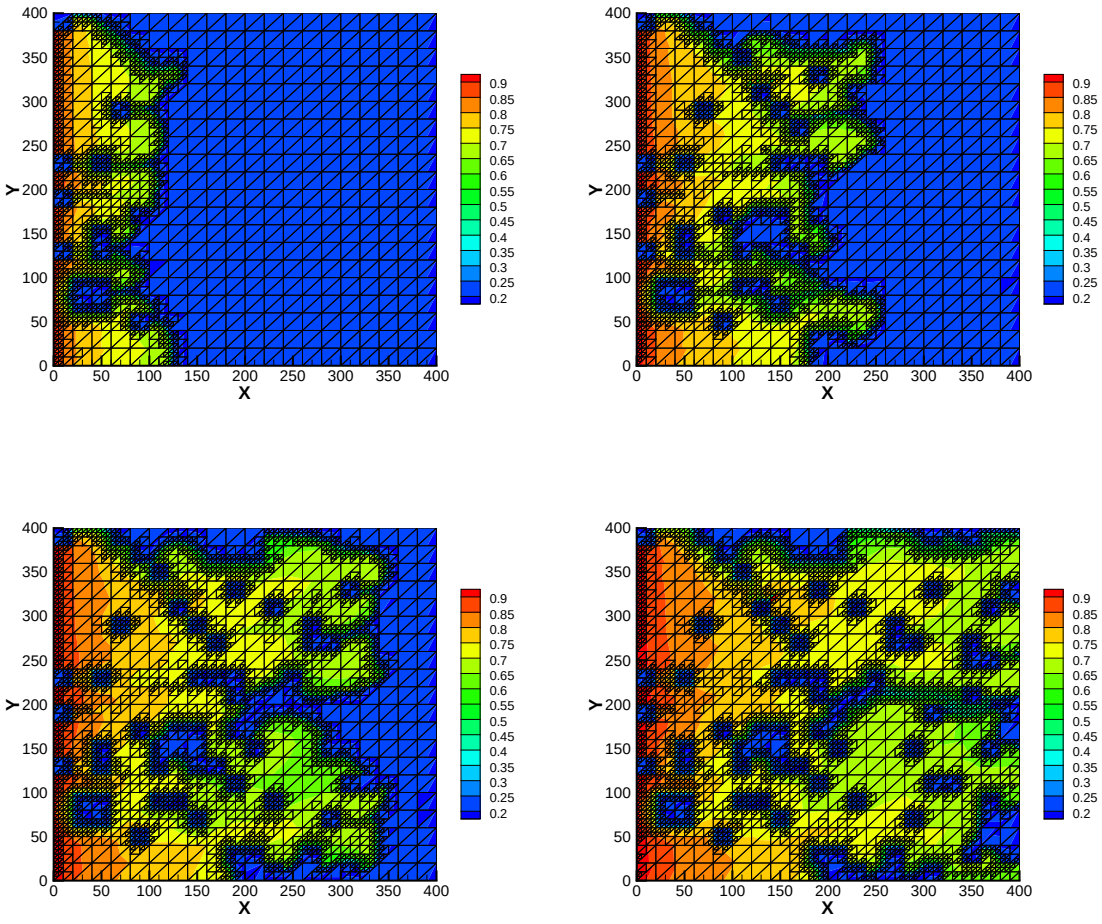

Fig. 15. Two-dimensional saturation contours at 17.5, 35, 52.5 and 70 days.

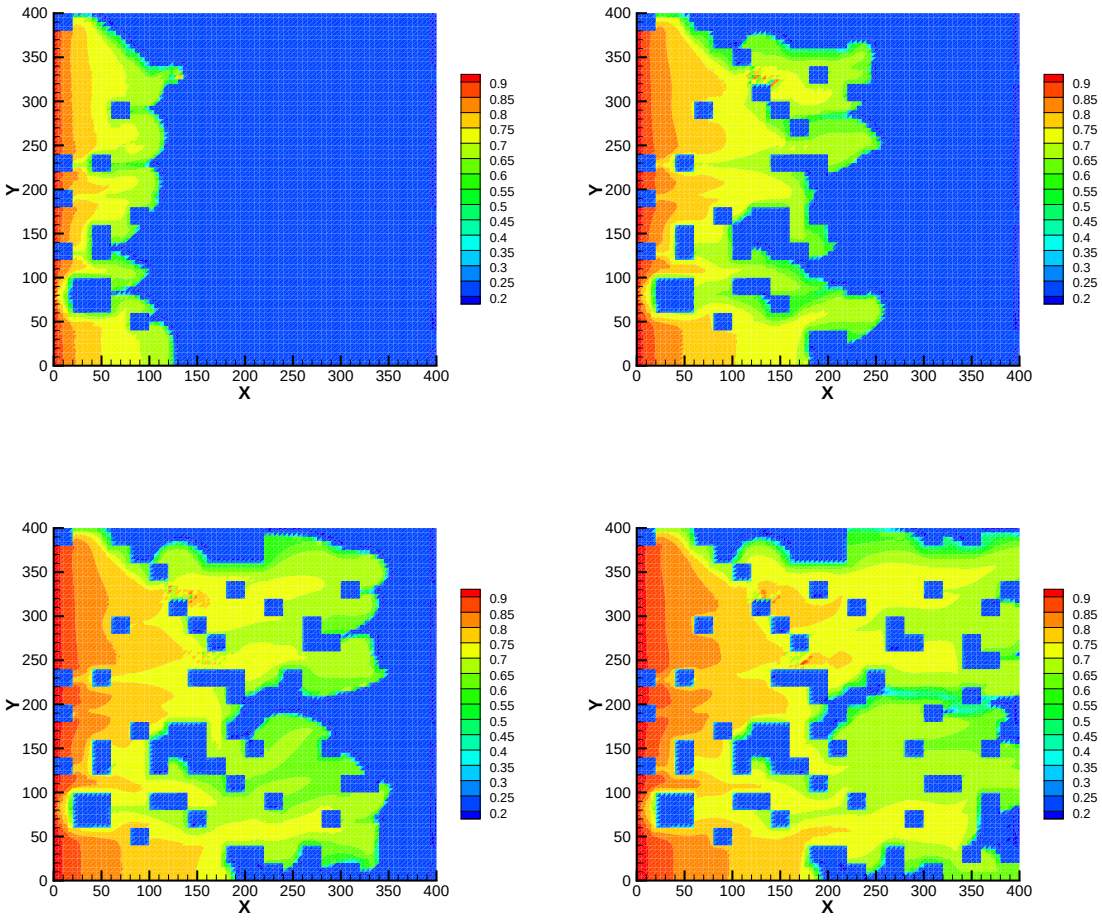

Fig. 16. Two-dimensional saturation contours at 17.5, 35, 52.5 and 70 days on uniform meshes.